The Role of Interfacial Tension in Nanobubble-Enhanced Oil Recovery

Ahmed Taman, Jan Kubelka, and Mohammad Piri*

Center of Innovation for Flow through Porous Media, Department of Energy and Petroleum Engineering, University of Wyoming, Laramie, Wyoming 82071, United States

Abstract. Aqueous nanobubble solutions (NBs) are emerging as promising enhanced oil recovery (EOR) agents due to their ability to improve oil displacement efficiency in geosystem applications. Unlike traditional EOR methods, which typically rely on chemical additives or complex gas formulations, NBs generated from accessible gases such as nitrogen offer a viable alternative. In this study, we examine the role of interfacial tension (IFT) in the displacement of different oils from porous media by NBs. To this end, we utilized mineral and crude oils with varying IFT with water to perform a series of elevated-pressure micromodel flooding experiments using NBs in a strongly oil-wet porous medium, whereas distilled water (DW) tests served as controls. NBs were prepared through a high-pressure generation system that combines membrane dispersion with microfluidic flow. IFT between each oil and both DW or NBs was measured to evaluate interfacial effects. Results show that NBs consistently enhanced sweep efficiency compared to DW, characterized by more uniform front propagation and reduced bypassed oil. This improvement was most pronounced in oils with higher IFT with water. The improved oil displacement by NBs is attributed to the reduction in oil-water IFT by NBs, which lowers the capillary forces and aids in the effective mobilization of oil.

1 Introduction

Aqueous nanobubble solutions (NBs) have recently emerged as promising agents for enhanced oil recovery (EOR), owing to their unique physicochemical properties [1–4]. Among the mechanisms proposed to explain the improved oil displacement by NBs, interfacial tension (IFT) reduction between oil and water has been recognized as a critical factor [2,5]. Aside from low-salinity water, IFT reduction in EOR has been achieved through the use of hazardous or high-cost chemicals, which pose both environmental and economic challenges [6,7]. As an alternative, NBs, especially those generated using readily available gases, offer a viable alternative [3,5].

Fluid displacement in porous media is affected by IFT, particularly under oil-wet conditions or within heterogeneous media, where capillary forces may dominate the flow behavior [8–12]. High IFT between the aqueous and oil phases results in significant capillary resistance, leading to the retention of large volumes of oil in the pore space [8]. From a pore-scale perspective, oil displacement occurs only when the capillary pressure (P_c) exceeds the threshold capillary pressure (P_{cth}) required to invade a pore. According to the Young–Laplace equation [13]:

$$P_{cth} = \frac{2\,\sigma \cos(\theta)}{r} \qquad (1)$$

where σ is the IFT, θ is the contact angle, and r is the pore radius, the P_{cth} is inversely proportional to the IFT. Therefore, lowering the IFT reduces this capillary barrier, and increases the capillary number (N_c) as expressed in Equation 2 [14]:

$$N_c = \frac{\mu_w\, v}{\sigma\, Cos\,(\theta)} \left(\frac{\mu_w}{\mu_o}\right)^{0.4} \qquad (2)$$

where μ_w and μ_o are the viscosity of the displacing and displaced phases, respectively, v is the Darcy velocity, and θ is the contact angle. The resulting rise in N_c enhances the ability of the aqueous phase to invade smaller pores and mobilize residual oil, leading to improved sweep efficiency, more uniform flood fronts, and higher oil recovery [15–17].

IFT reduction is a key target in many chemical EOR methods, including surfactant flooding [18–20], alkaline-surfactant-polymer (ASP) flooding [21–23], solvent injection [24], and more recently, nanoparticle-assisted flooding [25,26]. Surfactants reduce IFT by adsorbing at the oil–water interface, where their amphiphilic nature weakens interfacial forces between the two phases [18–20]. Alkaline agents react with acidic components in crude oil to generate in situ surfactants, which in turn decrease IFT [23]. Gases such as CO_2 and light alkanes reduce IFT by dissolving into the oil phase [27]. Nanoparticles, including silica, alumina, and metal oxides, can also lower IFT by adsorbing at the oil–water interface, forming interfacial films, and generating stable emulsions [25].

NBs are prepared by dispersing small volumes of gases, such as nitrogen, air, or CO_2, in water or brine, producing bubbles (nanobubbles) typically smaller than 1 µm in diameter [28,29]. Nanobubbles, in contrast to larger bubbles [30] or foams with high gas–liquid ratios [31,32],

---

* Corresponding author: ataman@uwyo.edu

demonstrate exceptional stability and can remain suspended in solution for weeks [33,34]. A variety of techniques have been developed to generate NBs, including cavitation, membrane dispersion, and microfluidic flow focusing [35–38]. Most of the tested methods operate under near-ambient pressure and temperature conditions, making them suitable for surface-level applications, such as wastewater treatment [39] and sand cleaning [40]. However, generation of nanobubbles under elevated pressure (i.e., conditions that better represent reservoir environments) remains scarce [5,41–43].

The small size of nanobubbles results in a significantly high surface-to-volume ratio, which enhances their interfacial activity and is believed to facilitate the reduction of IFT between the aqueous phase and oil [2,44,45]. However, the IFT reduction by NBs with oil has not been systematically investigated in the literature, and direct experimental evidence remains scarce. Only recently has it been demonstrated that N_2 NBs effectively reduce the IFT between the aqueous phase and oil compared to distilled water (DW) [5]. This was attributed to the inherent hydrophobicity of nanobubbles, which drives their preferential migration toward the oil–water interface and facilitates their dissolution into the oil phase.

In this study, we investigate the role of IFT in the displacement of various oils from strongly oil-wet porous media by NBs. A series of elevated-pressure micromodel flooding experiments were conducted with both mineral and crude oils, selected for their varying IFT values with the aqueous phase, while parallel DW flooding tests were performed as controls. NBs were generated through a novel high-pressure system that combines membrane dispersion with microfluidic flow, enabling the stable formation of nanobubbles. In addition, we examined the ability of NBs to break down disconnected oil ganglia and enhance their connectivity and subsequent mobilization through the pore network.

2 Material and methods

2.1 Fluids

DW served both as the base fluid for NB generation and as a control to evaluate NB performance. It was produced from tap water via a distillation system and transferred to sealed containers to prevent external contamination. To ensure its purity, the water was evaluated using nanoparticle tracking analysis (NTA) on the NanoSight Pro (Malvern Panalytical), confirming it contained no detectable bubbles or impurities.

NBs were produced under both low- and high-pressure conditions. High-pressure NBs (NBs$_{\text{HP}}$), generated at 200 psi [5], were utilized in all micromodel flooding experiments. For the IFT measurements, low-pressure NBs (NBs$_{\text{LP}}$) was prepared using a commercial NB generator. In both approaches, high-purity nitrogen gas (Airgas, 100%) served as the gas phase.

A reservoir crude oil, soltrol-170 (Chevron), and decane (99.9% purity, Sigma Aldrich) were selected as representative oil phases. Soltrol-170 was chosen specifically for its viscosity that closely matches that of the crude oil, allowing isolation of IFT effect, while decane, with its significantly lower viscosity than crude oil, was used to introduce a clear viscosity contrast (see Table 1). Prior to use, soltrol-170 was passed through successive layers of silica gel and alumina to remove reactive compounds, while decane, due to its high purity, was utilized without treatment. The crude oil was purified using a 0.5 µm stainless steel filter. To enable fluorescence-based imaging and segmentation, a trace amount of Nile Red dye (<0.00003 wt.%, Biotium) was added to both soltrol-170 and decane. No dye was required for the crude oil, as it exhibits natural fluorescence.

The density and viscosity of each fluid were measured under ambient conditions using the Anton Paar SVM 3001 viscometer (Table 1). For the NBs generated at elevated pressure (NBs$_{\text{HP}}$), samples were first collected through relief valves at atmospheric pressure and then left to stand for 10–15 minutes to allow microbubbles to escape from the solution before measurement. To verify the accuracy and consistency of the measurements, each sample was tested two to three times.

Table 1. Fluid properties (density and viscosity) measured under ambient conditions

Fluid	Density (g/mL)	Viscosity (cp)
DW	0.9976(1)^a	0.923(8)
NBs$_{\text{HP}}$	0.9975(1)	0.906(1)
NBs$_{\text{LP}}$	0.9976(1)	0.93(2)
Soltrol-170	0.7726(2)	2.677(1)
Decane	0.7286(1)	0.8732
Crude oil	0.815(2)	2.48(2)

^{a}Mean values with the standard deviation in the last digit given in parentheses.

2.2 Micromodel

A uniform pore network micromodel made of glass (Micronit) was employed in all flooding experiments (Figure 1). Stainless steel Swagelok fittings (1/16") were

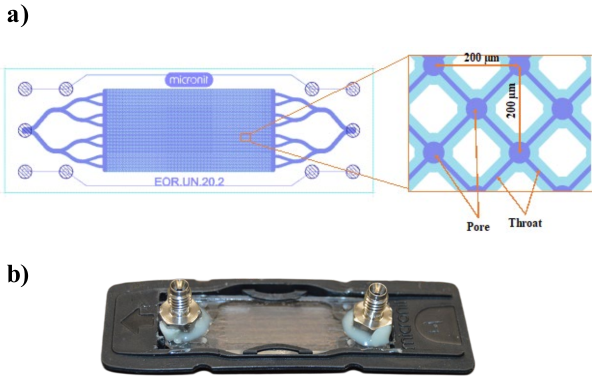

Fig. 1. The micromodel employed in oil flooding experiments: a) schematic diagram [46], and b) a real image captured after attaching the metal inlet and outlet fittings.

connected to the inlet and outlet ports to ensure chemical compatibility and high-pressure tolerance [5]. The absolute permeability of the micromodel was measured by injecting distilled water (DW) at 200 psi under varying flow rates, while recording the pressure drop using a differential pressure transducer. The obtained permeability value was 2.57 Darcy, which was in agreement with the manufacturer's specifications [46].

The wettability of the micromodel was modified from strongly water-wet to strongly oil-wet through silanization [47,48], resulting in an equilibrium in-situ oil–DW contact angle of approximately 151° ± 6 (see Figure 2), compared to 45° [5] prior to treatment. Contact angle measurements showed no significant variation between DW and NB tests for any of the oils.

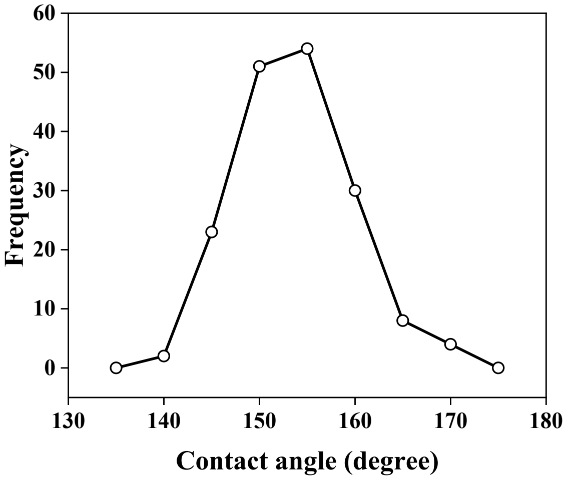

Fig. 2. In-situ contact angle distribution measured at multiple locations within the porous medium at the end of flooding for both DW and NB experiments (172 measurements in total).

2.3 NB generation and characterization

NBs$_{SLP}$ were produced by a customized XTB-25 nanobubble generator (Moleaer Inc.) [3], equipped with a 25-gallon tank. The N_2 injection rate was 0.5 ft^3/hr and the solution was continuously circulated at 25 gallons per minute for one hour. The NBs$_{SHP}$ were generated by combining membrane dispersion [49] and microfluidic flow focusing [50]. The N_2 and DW were co-injected through a stainless-steel membrane with pore sizes ranging from <1 µm to ~50 µm under a pressure of 200 psi [5], and subsequently passed through a micromodel, originally built for a separate study [51]. The micromodel improved the quality of the high-pressure generated NBs, as indicated by their higher concentration and smaller size [5].

Several gas-liquid ratios were tested to identify the optimal NBs$_{SHP}$ for oil flooding experiments. For each case, samples were collected both before and after passing through the micromodel and analyzed.

Nanobubble size and concentration were determined by NTA, and zeta potential by Zetasizer (both Malvern Panalytical). Passing the NB solution through micromodel consistently increased the nanobubble concentration, as confirmed by both NTA and zeta potential measurements [5]. NBs collected from the final sampling point prior to flooding exhibited a median size of 86 nm, a concentration of 1.8×10^8 bubbles/mL, and a zeta potential of −32 ± 4 mV (Figure 3).

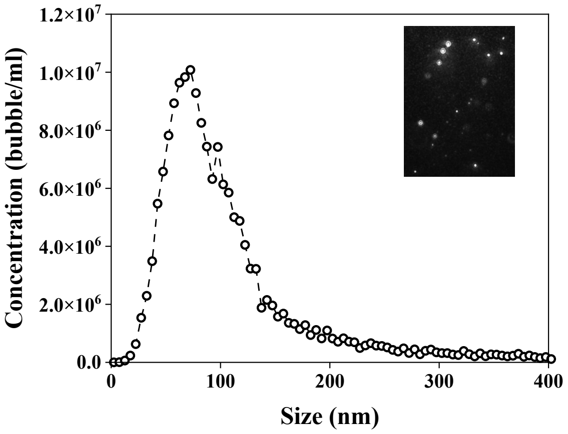

Fig. 3. Average size distribution of high-pressure generated nanobubbles (NBs$_{HP}$) collected prior to oil flooding. Inset: Representative NTA snapshot showing individual nanobubbles as white circles.

2.4 Experiments

2.4.1 Micromodel flooding

To evaluate the effectiveness of NBs, a series of micromodel flooding tests were conducted using DW as a reference. Each experiment was conducted twice to ensure reproducibility, resulting in a total of 12 tests.

The experimental setup consists of two main sections: a high-pressure NB generation system and a micromodel flooding setup. The flooding part included two Quizix 5K pumps (P_3 for DW injection and P_4 for backpressure control). A syringe pump (Harvard Apparatus) was used to clean the lines and the micromodel following each test. The micromodel was fully saturated with oil by injecting it through a high-pressure accumulator connected to a N_2 gas cylinder. Pressure drop was continuously monitored using a Rosemount pressure transmitter, while an Olympus IX83 microscope captured real-time images of oil displacement.

Prior to the flooding experiments, NBs were prepared and collected in a high-pressure cell approximately 14 hours in advance. The cell was kept under a N_2 blanket at 200 psi for 12 hours, allowing it to fill nearly to capacity. An additional 2-hour stabilization period followed, during which no liquid was introduced, ensuring the NBs remained stable under pressure. The generated NBs were then transferred from the pressure cell to the accumulator using pump P_3 and a N_2-pressurized cylinder, maintaining constant pressure. Meanwhile, the micromodel was vacuumed for about one hour at −10 psi to remove trapped gases, then fully saturated with oil at 200 psi using a pressurized N_2 cylinder and a high-pressure accumulator.

Before the start of oil flooding, the NB solution was pumped at 200 psi using P_3 to displace the fluids and then were introduced into the micromodel. Throughout the process, the backpressure pump (P_4) collected the produced fluids while maintaining a constant pressure of 200 psi. In all tests, the injection rate for both DW and NBs was kept at 0.0002 mL/min, corresponding to capillary numbers of ranges from 3.4×10^{-7} to 5.7×10^{-7}, respectively (see below Table 2).

The porous medium was imaged using a microscope operating in Fluorescein Isothiocyanate (FITC) mode, with images captured every two minutes. The raw grayscale images were processed in ImageJ, where they were cropped and aligned prior to further analysis. The pre-processed images were then imported into Avizo, where interactive thresholding was applied to segment the pores from the solid grains. The oil phase was also segmented using the same thresholding method, enabling the calculation of oil saturation (S_o) and recovery over time. Additional experimental details can be found in another study [5].

2.4.2 Interfacial tension

IFT between all oils and either DW or NBs was determined using the captive drop method in a Hastelloy cell [52,53]. The cell was first filled with DW and NB solutions to conduct DW/oil and NB/oil measurements, respectively. A stainless-steel needle was used to inject the oil phase from the bottom of the cell, forming a droplet. A needle with an outer diameter of 3.05 mm was used for the IFT measurements with soltrol-170 and decane, while for the crude oil the IFT was obtained with a 2.73 mm needle to ensure droplet stability. This setup achieved equilibrium bond numbers ranging from 0.57 to 0.70 for both DW/oil and NB/oil systems. To ensure reproducibility, at least two trials were carried out for each case.

3 Results and discussion

3.1 Micromodel flooding

First, we present the fluid occupancies at the end of DW and NB flooding experiments (Figure 4). In all tests, flooding was continued until ~25 pore volumes (PVs) were injected, or earlier if no additional oil recovery was observed. The final captured images were then segmented to calculate oil recovery. In the case of decane, however, the tests were extended beyond 100 PV, as a pronounced increase in oil production was observed in the NB experiments after breakthrough. The injected PV was calculated from the point at which the aqueous phase first appeared in the field of view (FOV), using the pump rate to determine the subsequent volume.

In all experiments, NB flooding consistently outperformed DW Injection, demonstrating improved sweep efficiency as evidenced by more uniform front propagation and reduced bypassed oil (Figures 4 and 5). The final recovery factors (RF) for DW flooding were measured as 41.3 ± 0.9% for soltrol-170, 79 ± 2.3% for crude oil, and 71.6 ± 0.7% for decane. In comparison, NB flooding resulted in RFs of 65 ± 3% for soltrol-170, 85 ± 2% for crude oil, and 82 ± 3% for decane. These values correspond to approximate improvements in oil recovery of 50%, 7%, and 14%, respectively.

Evidently, the flooding behavior in the soltrol-170 scenario (Figure 4a) was notably different from that observed with crude oil and decane. In particular, DW injection led to inefficient displacement, with a significant portion of oil bypassed. By contrast, NBs propagated more uniformly through the porous medium, resulting in greater oil recovery. This improved performance can be attributed to the combined impact of viscosity ratio differences and IFT reduction by NBs.

The overall lowest recovery by DW was recorded in the soltrol-170 case, where the large viscosity contrast between the aqueous and oil phases caused water to travel faster toward the outlet, leaving a significant volume of oil unrecovered. Although crude oil had a similar viscosity to soltrol-170, it was displaced more effectively by DW due to the lower IFT. Decane, despite having the highest IFT with water, exhibited higher recovery than soltrol-170, primarily due to its comparable viscosity to the aqueous phase (see Table 1).

Since the viscosity of NBs is similar to that of DW (Table 1), the enhanced oil recovery observed with NBs can be primarily attributed to their ability to reduce IFT, as discussed in detail in Section 3.2.

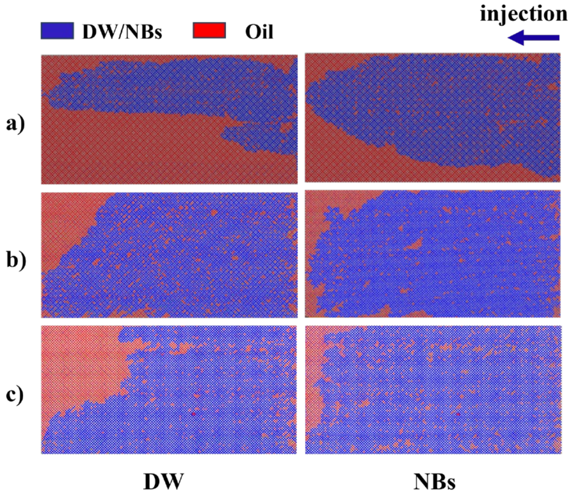

Fig. 4. Representative fluid occupancy maps at the end of flooding for each case: (a) soltrol-170, (b) crude oil, and (c) decane.

On a closer examination, the RF evolution over time revealed a delayed breakthrough (BT) in the NB flooding experiments. As shown in the representative results (Figure 6), BT occurred after injecting approximately 2.5 PV of NBs during the soltrol-170 flooding, compared to just 0.7 PV for DW. A similar delay was noted in the crude oil case, with BT occurring after ~1.7 PV of NB injection versus ~1 PV for DW. For decane, BT was reached at ~1 PV with NBs, while DW flooding resulted in BT after injecting ~0.7 PV.

This delayed breakthrough is attributed to the compressibility of NBs [5,54], which required a longer

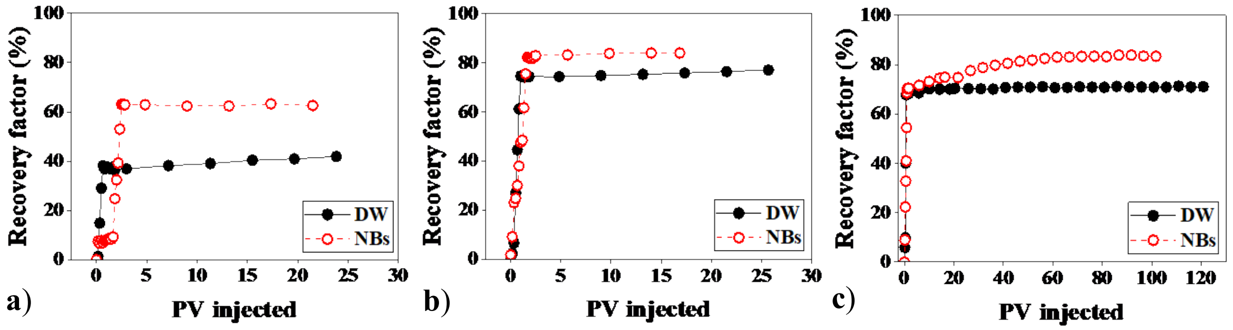

Fig. 6. RF as a function of injected pore volume (PV) for both DW and NB flooding scenarios: (a) soltrol-170, (b) crude oil, and (c) decane.

time to reach the P_{cth} necessary for invading the pores. Additionally, the strong affinity of NBs toward the oil phase may have slowed their advancement toward the outlet, instead promoting their preferential propagation across the width of the porous medium (see Figure 4). In line with this observation, lower pressure drops (ΔPs) were recorded for NBs either upon entering the pore elements (Figure 7a) or shortly afterwards (Figure 7b, c), compared to DW. The reduced ΔPs reflect the ability of NBs to lower capillary barriers by reducing the IFT, as further discussed in Section 3.2.

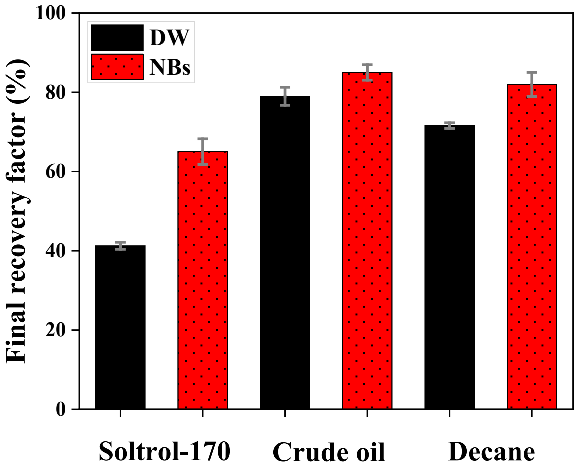

Fig. 5. Final oil recovery factors averaged for DW and NB flooding experiments. Error bars denote the standard deviation calculated from individual tests.

3.2 Interfacial tension

NBs decreased the IFT between the aqueous phase and the various oils used in this study, relative to water (Figure 8, Table 2). The measured IFT reductions achieved by NBs (Table 2) were approximately 12%, 6%, and 18% for soltrol-170, crude oil, and decane, respectively. A more pronounced reduction in IFT was observed for oils exhibiting higher oil–water IFT. Although the maximum IFT reduction observed (~18%) is considerably smaller than what is typically achieved with surfactants [18–20], it may still contribute meaningfully to oil recovery [5]. It is also important to note that these IFT measurements were performed under ambient conditions using NBs generated at low pressure (NBs_{LP}), which may not fully represent the behavior of NBs under the higher-pressure conditions during oil flooding. Under elevated-pressure conditions, the application of NBs_{HP} is expected to have a greater impact, as these solutions likely contain a higher concentration of gas [41,42] (both dissolved and dispersed), which can further reduce the interfacial barrier between oil and the NBs.

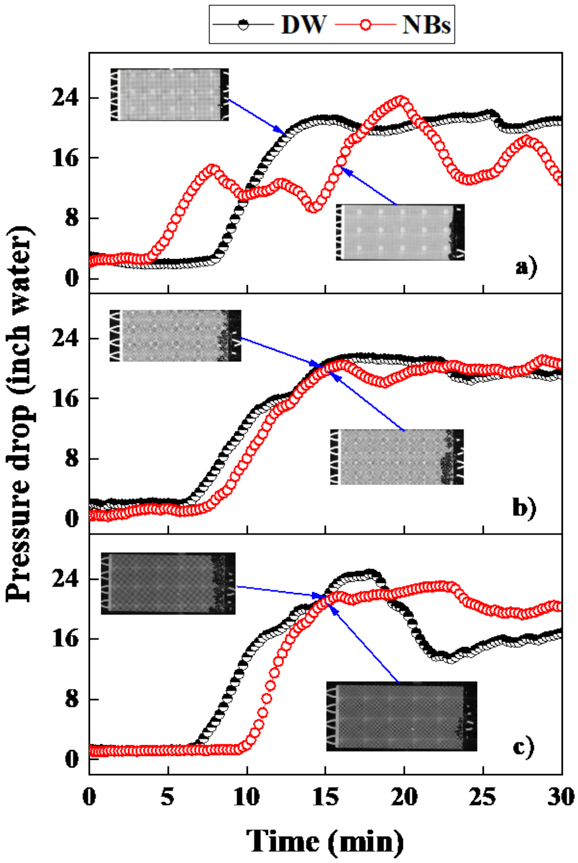

Fig. 7. Pressure drop evolution over time following the injection of ~ 1 PV, considered from the time the invading phase entered the pore space, for: (a) soltrol-170, (b) crude oil, and (c) decane. The accompanying images show grayscale snapshots captured during flooding, where white represents oil and black corresponds to the aqueous phase (DW or NBs).

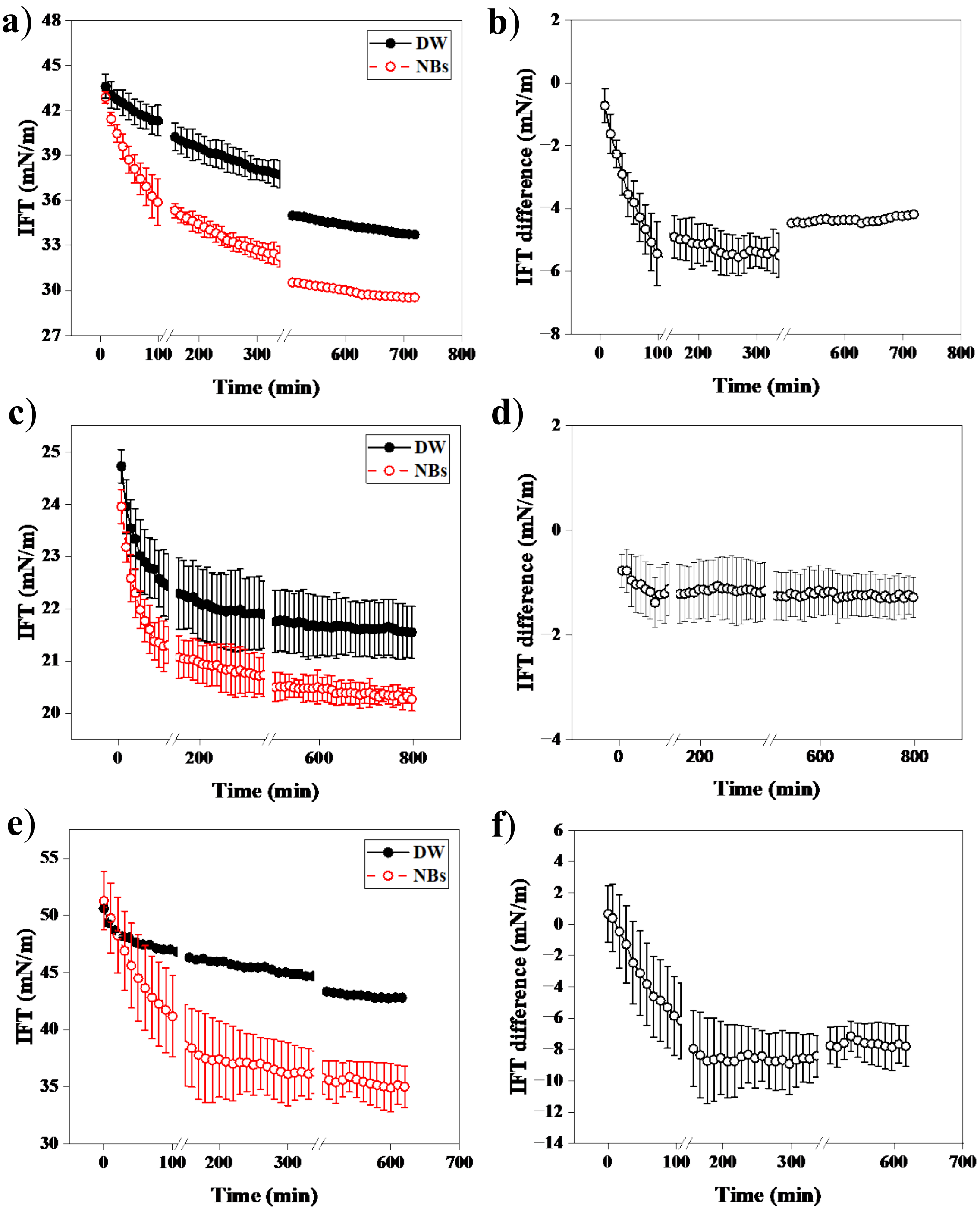

Fig. 8. Variations in IFT over time for NB/oil and DW/oil systems. Plots (a), (c), and (e) show IFT values measured over time for soltrol-170, crude oil, and decane, respectively. Corresponding difference plots between NB/oil and DW/oil systems are shown in (b), (d), and (f). Error bars represent the standard deviation from independent measurements.

Table 2. IFT values, capillary numbers (N_c), and viscosity ratios (M) for the fluid systems tested.

Fluids		Mean IFT (mN/m)	$N_c^* \times 10^{-7}$	M
Non-aqueous	Aqueous			
Soltrol-170	DW	33.7	3.4	0.34
	NBs	29.5	3.8	0.33
Crude oil	DW	21.6	5.5	0.37
	NBs	20.3	5.7	0.36
Decane	DW	42.7	4.3	1.06
	NBs	35	5.1	1.04

* N_c computed using Equation 2.

Oil recovery is affected by several fundamental parameters, including wettability, IFT, and viscosity ratio between the displacing and displaced phases [8,12,55]. In this study, the micromodel wettability remained consistent across all flooding experiments, as confirmed by the small variations observed in the in-situ contact angle measurements (see Figure 2). While wettability remained unchanged, the IFT varied among the three oils, and the viscosity ratio was comparable only between soltrol-170 and crude oil (Table 2). Given the low N_c observed in these experiments, the displacement occurred under conditions within or close to the capillary fingering regime (see Figure 9), where capillary forces dominate and viscous forces have minimal impact [14,16]. In general, the residual oil saturation (S_{or}) declined as N_c increased for both DW and NB flooding scenarios (Figure 10a). On the other hand, no clear relationship was observed between S_{or} and M (Figure 10b). It is evident that NBs, when compared to DW, effectively raised N_c in experiments with the various oils tested (Figure 10a and Table 2), which in turn led to a decrease in S_{or} across all cases (Figure 10a, 5).

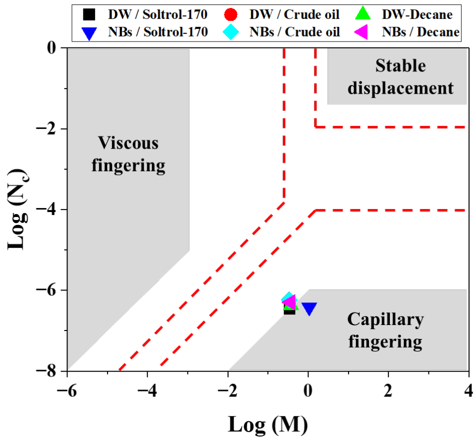

Fig. 9. Displacement regime map based on Lenormand's phase diagram [16] (adapted from Zacharoudiou et al. [56]). Gray regions represent flow regimes identified through simulations by Lenormand et al. [16], while red dashed lines denote experimental boundaries reported by Zhang et al [57].

Nevertheless, similar M values for soltrol-170 and crude oil, provide an opportunity to isolate and investigate the specific impact of IFT on additional oil recovery by NBs. Since other influencing parameters were held constant, differences in recovery can be more confidently attributed to IFT variations. Markedly, the greater reduction in IFT achieved by NBs for soltrol-170 compared to crude oil (Figure 8a-d) corresponded to a greater improvement in oil recovery relative to their respective DW flooding base cases.

By contrast, decane displacement exhibited a similar trend between DW and NB flooding before the breakthrough, with NBs achieving slightly higher recovery than DW (Figure 6c). However, after breakthrough, NBs produced significantly larger amount of oil, which was not observed in the DW tests. This trend resulted from the delayed IFT reduction by NBs (Figure 8e, f), compared to DW, which over time promoted the invasion of the aqueous phase into additional pores and thereby enhanced oil mobilization.

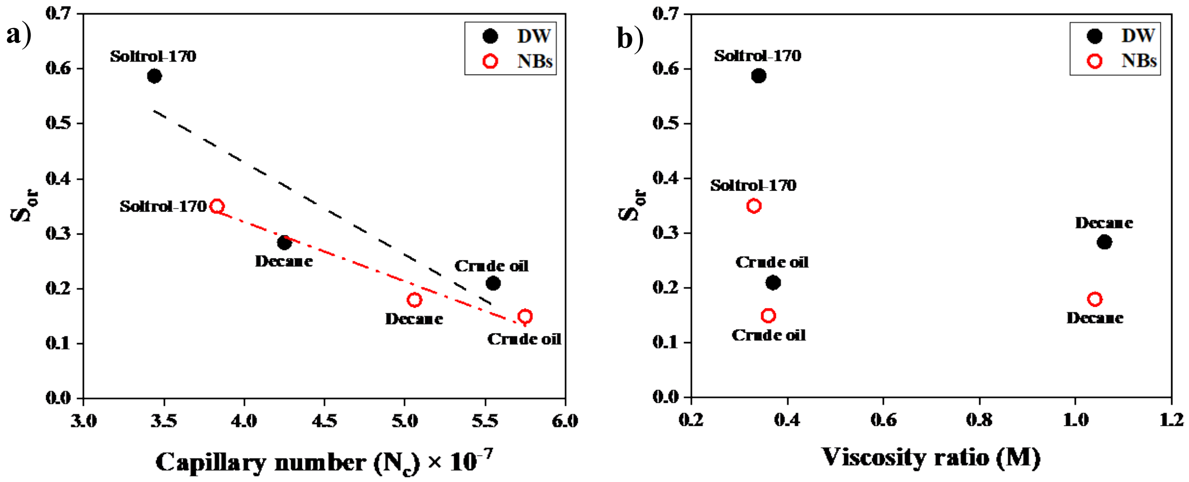

Fig. 10. Relationship between S_{or} and (a) capillary number and (b) viscosity ratio.

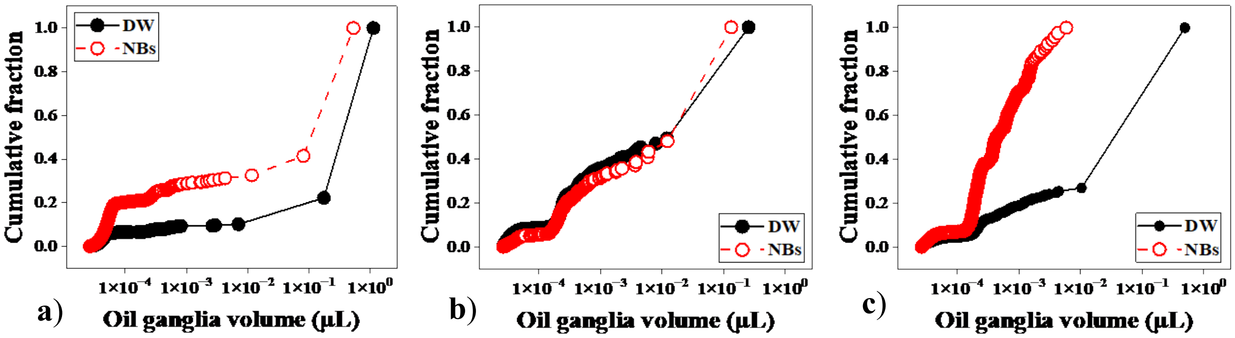

Fig. 11. Comparison of cumulative fractions of residual oil ganglia volumes after flooding for representative experiments with: (a) soltrol-170, (b) crude oil, and (c) decane.

In light of the observed IFT reduction by NBs compared to water, we further evaluated the size distribution of the residual oil globules remaining in the porous medium after flooding. The final segmented images from a representative experiment for each oil type were analyzed using Avizo software. The cumulative fractions were then computed and plotted against the corresponding oil ganglia volumes [48,58] (Figure 11).

Overall, NBs promoted the breakup of larger oil globules into smaller ones more effectively than DW flooding, likely due to the reduced IFT that weakens the capillary forces responsible for stabilizing larger oil droplets within the pore space [59,60]. This effect was particularly evident in decane and soltrol-170 experiments, where a greater reduction in residual oil globule size was observed compared to DW injection (Figure 11a,c). Unlike soltrol-170 and decane, crude oil showed a small difference between NB and DW cases, with similar volumes of remaining oil droplets at the end of flooding (Figure 11b). This limited improvement can be explained by the relatively smaller reduction in oil–water IFT achieved for crude oil relative to those of the other oils (Figure 8).

Moreover, the connectivity of the residual oil throughout the entire flooding process was evaluated. To this end, Euler number was calculated using Aviso for all segmented oil images of one representative experiment. The Euler number is a topological metric that reflects how well a fluid phase is connected, independent of its shape [61,62]. These values were then normalized using Equation 3:

$$E_N = \frac{E_{min} - E_{image}}{E_{min} - E_{max}} \qquad (3)$$

where E_N represents the normalized Euler number, E_{min} is the minimum Euler number calculated within a given experiment, E_{image} is the Euler number of the image being analyzed, and E_{max} is the maximum Euler number recorded during the experiment. E_N values were then plotted against the corresponding S_o to assess changes in oil phase connectivity during flooding (Figure 12). The average E_{min} values were approximately −10,300 ± 400 and −10,300 ± 600 for the DW and NB tests, respectively, corresponding to the initial state where the porous medium was fully saturated with oil. By contrast, the average E_{max} values were 1,200 ± 700 and 1,100 ± 700 for DW and NBs, respectively, representing the late stages of flooding when the oil globules are mostly disconnected within the porous medium.

At the start of flooding, when values were close to 1, the difference in E_N between NBs and DW was minimal. However, as injection progressed and S_o decreased toward residual levels, the gap between NB and DW cases became more pronounced. Overall, the results indicate that NBs consistently produced lower values at the same S_o compared to DW flooding, suggesting higher oil connectivity during displacement.

4 Conclusions

Nitrogen nanobubble solutions (NBs) enhanced the displacement efficiency in strongly oil-wet porous media under elevated-pressure conditions. Compared to distilled water (DW), NBs consistently improved sweep efficiency, delayed breakthrough, and achieved higher

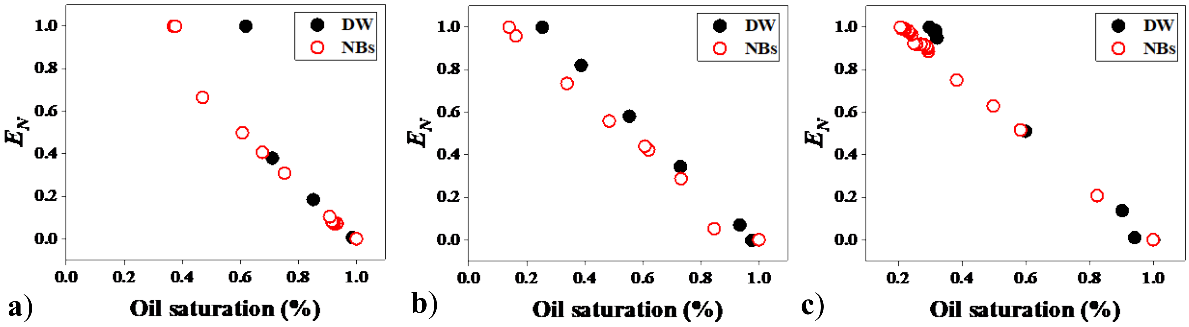

Fig. 12. Change in the normalized Euler number (E_N) as a function of oil saturation (S_o) during the displacement process for: (a) soltrol-170, (b) crude oil, and (c) decane.

final oil recovery, particularly for oils with higher oil–water IFT. The improved performance of NBs is attributed to their ability to reduce IFT, thereby lowering capillary barriers and promoting more uniform fluid front propagation. Micromodel experiments further revealed that NBs facilitated the fragmentation of larger residual oil globules into smaller ones and maintained higher oil phase connectivity throughout flooding, both of which contributed to reduced residual oil saturation.

The authors gratefully acknowledge the financial support of Hess Corporation and the University of Wyoming.

5 References

1. K Ohgaki, N.Q. Khanh, Y. Joden, A. Tsuji, T. Nakagawa, Chem. Eng. Sci. **65**, 1296–1300 (2010).
2. L. Cai, J. Wu, M. Zhang, K. Wang, B. Li, X. Yu, et al. Nanomaterials **14**, 1280 (2024).
3. H. Elnaggar, A. Taman, R. Ali, M. Arshadi, D. Joshi, S.F.K. Joy, et al. Energy Fuels (2025).
4. T. Lawal, H. Wang, A. Mirzaei-Paiaman, R. Okuno, *SPE Improved Oil Recovery Symp.* (2024).
5. A. Taman, A.E. Shoukry, J. Kubelka, M. Piri, J. Colloid Interface Sci. **693**, 137647 (2025).
6. A.O. Gbadamosi, R. Junin, M.A. Manan, A. Agi, A.S. Yusuff, Int. Nano Lett. **9**, 171–202 (2019)
7. J.K. Borchardt, Kirk-Othmer Encycl, Enhanced Oil Recovery, Chem. Technol., Vol. **18** (2000)
8. M.J. Blunt, *Multiphase Flow in Permeable Media* (Cambridge University Press, 2016)
9. W. Xu, J.T. Ok, F. Xiao, K.B. Neeves, X. Yin, Phys. Fluids **26** (2014)
10. R.I. Al-Raoush, C.S. Willson, J. Contam. Hydrol. **77**, 67–89 (2005)
11. I. Chatzis, N.R. Morrow, H.T. Lim, SPE J. **23**, 311–326 (1983)
12. F.A.L. Dullien, Porous media : fluid transport and pore structure, Elsevier, **5–74** (1979)
13. S.M. Hassanizadeh, W.G. Gray, Water Resour. Res. **29**, 3389–3405 (1993).
14. A. Abrams, SPE J. **15**, 437–447 (1975)
15. L. Lake, R.T. Johns, W.R. Rossen, G.A. Pope, *Fundamentals of Enhanced Oil Recovery* (SPE, 2014)
16. R. Lenormand, E. Touboul, C. Zarcone, J. Fluid Mech. **189**, 165–187 (1988)
17. B. Zhao, C.W. MacMinn, B.K. Primkulov, Y. Chen, A.J. Valocchi, J. Zhao, et al., Proc. Natl. Acad. Sci. USA **116**, 13799–13806 (2019)
18. E.G. Schwarz, W.G. Reid, Ind. Eng. Chem. **56**, 26–31 (1964)
19. O. Massarweh, A.S. Abushaikha, Energy Rep. **6**, 3150–3178 (2020)
20. G.J. Hirasaki, C.A. Miller, M. Puerto, *SPE Annu. Tech. Conf. Exhib.* (2008)
21. M.S. Numin, A. Hassan, K. Jumbri, A. Ramli, N. Borhan, J. Mol. Liq. **356**, 119006 (2022)
22. A.A. Olajire, Energy **77**, 963–982 (2014)
23. J.J. Sheng, *Modern Chemical Enhanced Oil Recovery* (Elsevier, 2011)
24. I. Nowrouzi, A.H. Mohammadi, A.K. Manshad, J. Mol. Liq. **304**, 112733 (2020)
25. N.A. Ogolo, O.A. Olafuyi, M.O. Onyekonwu, *SPE Saudi Arabia Sect. Tech. Symp. Exhib.* (2012)
26. Y.E. Kandiel, F.I. Metwalli, R.E. Khalaf, G.M. Attia, O. Mahmoud, *Mediterranean Offshore Conf.* (2024)
27. N. Choudhary, A.K. Narayanan Nair, M.F.A. Che Ruslan, S. Sun, Sci. Rep. **9**, 19784 (2019)
28. K. Yasuda, H. Matsushima, Y. Asakura, Chem. Eng. Sci. **195**, 455–461 (2019)
29. B. Singh, G. Park, J.H. Ryu, M.H. Park, Appl. Sci. (Switz.) **15** (2025).
30. A. Upadhyay, S.V. Dalvi, Ultrasound Med. Biol. **45**, 301–343 (2019).
31. A. Aboahmed, K. Mohanty, *SPE Int. Conf. Oilfield Chem.* (2025).
32. M.I. Youssif, M. Piri, L. Goual, Energy Fuels **38**, 15887–15912 (2024).
33. L.J. Zhang, H. Chen, Z.X. Li, H.P. Fang, J. Hu, Sci. China Ser. G Phys. Mech. Astron. **51**, 219–224 (2008)
34. F.Y. Ushikubo, T. Furukawa, R. Nakagawa, M. Enari, Y. Makino, Y. Kawagoe, et al., Colloids Surf. A Physicochem. Eng. Asp. **361**, 31–37 (2010)
35. A. Agarwal, W.J. Ng, Y. Liu, Chemosphere **84**, 1175–1180 (2011)
36. M. Alheshibri, J. Qian, M. Jehannin, V.S.J. Craig, Langmuir **32**, 11086–11100 (2016)
37. C. Wu, K. Nesset, J. Masliyah, Z. Xu, Adv. Colloid Interface Sci. **179–182**, 123–132 (2012)
38. X. Li, B. Peng, Q. Liu, J. Liu, L. Shang, Fuel **341**, 127661 (2023)
39. T. Temesgen, T.T. Bui, M. Han, T. il Kim, H. Park, Adv. Colloid Interface Sci. **246**, 40–51 (2017)
40. T.T. Bui, C.D. Nguyen, N. Shim, M. Han, Environ. Nanotechnol. Monit. Manag. **17**, 100653 (2022)
41. H. Wang, T. Lawal, S.H. Achour, K. Sheng, R. Okuno, Energy & Fuels **37**, 19726–19737 (2023)
42. S.H. Achour, T. Lawal, K. Sheng, R. Okuno, (2024)
43. T. Lawal, H. Wang, R. Okuno, J. Mol. Liq. **398**, 124340 (2024)
44. K. Yasui, T. Tuziuti, N. Izu, W. Kanematsu, Ultrason. Sonochem. **52**, 13–18 (2019)
45. W. Shen, D. Mukherjee, N. Koirala, G. Hu, K. Lee, M. Zhao, et al. Environ. Rev. **30**, 359–379 (2022)
46. EOR Information, Enhanced Oil Recovery Overview, Micronit
47. M.H. Sedaghat, M.H. Ghazanfari, M. Masihi, D. Rashtchian, J. Pet. Sci. Eng. **108**, 370–382 (2013)
48. A.E. Shoukry, S. Saraji, M. Piri, J. Hydrol. **631**, 130748 (2024)
49. A.K.A. Ahmed, C. Sun, L. Hua, Z. Zhang, Y. Zhang, W. Zhang, et al. Chemosphere **203**, 327–335 (2018).
50. S.A. Peyman, J.R. McLaughlan, R.H. Abou-Saleh, G. Marston, B.R.G. Johnson, S. Freear, et al. Lab Chip **16**, 679–687 (2016).
51. A.E. Shoukry, A. Taman, S. Saraji, M. Piri, Unpublished results.
52. V. Mirchi, S. Saraji, L. Goual, M. Piri, Fuel **148**, 127–138 (2015)

53. S. Saraji, L. Goual, M. Piri, H. Plancher, Langmuir **29**, 6856–6866 (2013)
54. A. Telmadarreie, A. Doda, J.J. Trivedi, E. Kuru, P. Choi, J. Pet. Sci. Eng. **138**, 160–173 (2016)
55. C. Huang, X. Dai, C. Shi, L. Shi, J. Therm. Sci. **30**, 2137–2149 (2021)
56. I. Zacharoudiou, E.S. Boek, J. Crawshaw, Water Resour. Res. **56** (2020)
57. C. Zhang, M. Oostrom, T.W. Wietsma, J.W. Grate, M.G. Warner, Energy & Fuels **25**, 3493–3505 (2011)
58. B. Zhang, A.I.A. Mohamed, L. Goual, M. Piri, Sci. Rep. **10**, 17539 (2020).
59. R. Lenormand, C. Zarcone, A. Sarr, J. Fluid Mech. **135**, 337 (1983)
60. W. Yang, J. Lu, B. Wei, H. Yu, T. Liang, ACS Omega **6**, 6064–6069 (2021)
61. S. Khorsandi, L. Li, R.T. Johns, SPE J. **22**, 1915–1928 (2017).
62. A.L. Herring, E.J. Harper, L. Andersson, A. Sheppard, B.K. Bay, D. Wildenschild, Adv. Water Resour. **62**, 47–58 (2013).